

Supporting Information

for *Adv. Funct. Mater.*, DOI: 10.1002/adfm.202202204

AlScN-on-SiC Thin Film Micromachined Resonant
Transducers Operating in High-Temperature
Environment up to 600 °C

*Wen Sui, Haoran Wang, Jaesung Lee, Afzaal Qamar,
Mina Rais-Zadeh, and Philip X.-L. Feng**

AlScN-on-SiC Thin-Film Micromachined Resonant Transducers**Operating in High-Temperature Environment up to 600°C**

Wen Sui¹, Haoran Wang¹, Jaesung Lee¹, Afzaal Qamar²,

Mina Rais-Zadeh^{2,3}, Philip X.-L. Feng^{1*}

¹*Department of Electrical and Computer Engineering, Herbert Wertheim College of Engineering,
University of Florida, Gainesville, FL 32611, USA*

²*Department of Electrical Engineering & Computer Science,
University of Michigan, Ann Arbor, MI 48109, USA*

³*NASA Jet Propulsion Laboratory, California Institute of Technology, Pasadena, CA 91109, USA*

Table of Contents

- 1. XRD Analysis of the AlScN/SiC/Si Heterostructure**
- 2. TEM Imaging of the AlScN/SiC Interface**
- 3. Temperature Coefficient of Resonance Frequency (TC_f) of Circular Diaphragm**
 - 3.1. Tension Dominant Limit
 - 3.2. Flexural Rigidity Dominant Limit
- 4. Temperature Calibration Based on Si Raman Thermometry**
- 5. Raman Spectroscopy Measurement with Varying Temperature**

1. XRD Analysis of the AlScN/SiC/Si Heterostructure

Single-crystal n-type 3C-SiC (100) thin film with the thickness of 900 nm is grown on the Si (100) substrate by low pressure chemical vapor deposition (LPCVD) process. 1 μm -thick AlScN with 20% Sc is then sputtered on the 3C-SiC/Si substrate. After the growth process, x-ray diffraction (XRD) analysis of the grown film is carried out to confirm the crystal structure. **Figure S1** shows the XRD measurement results of the AlScN/3C-SiC/Si heterostructure obtained in conventional θ - 2θ scan mode. We observe the peaks corresponding to the (100) plane for the SiC thin film, which indicates that single-crystal 3C-SiC (100) is grown on Si (100). Three peaks are observed for AlScN, which confirms the polycrystalline nature with the preferred orientation along the c -axis, *i.e.*, AlScN (002) peak.

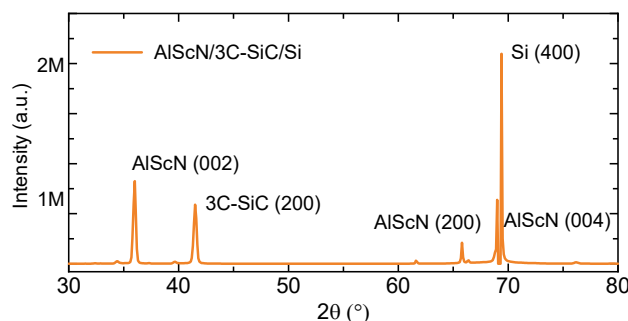


Figure S1. XRD analysis of the AlScN/3C-SiC/Si heterostructure.

2. TEM Imaging of the AlScN/SiC Interface

Figure S2a shows the transmission electron microscopy (TEM) image of the AlScN/SiC interface, which shows the columnar growth of AlScN. Grain boundaries are not observed in the 3C-SiC thin film; and the only defects are stacking faults. The selected area electron diffraction (SAED) pattern (Figure S2b-e) reinforces the XRD results and confirms that the 3C-SiC thin film is single-crystalline, and the AlScN thin film is polycrystalline.

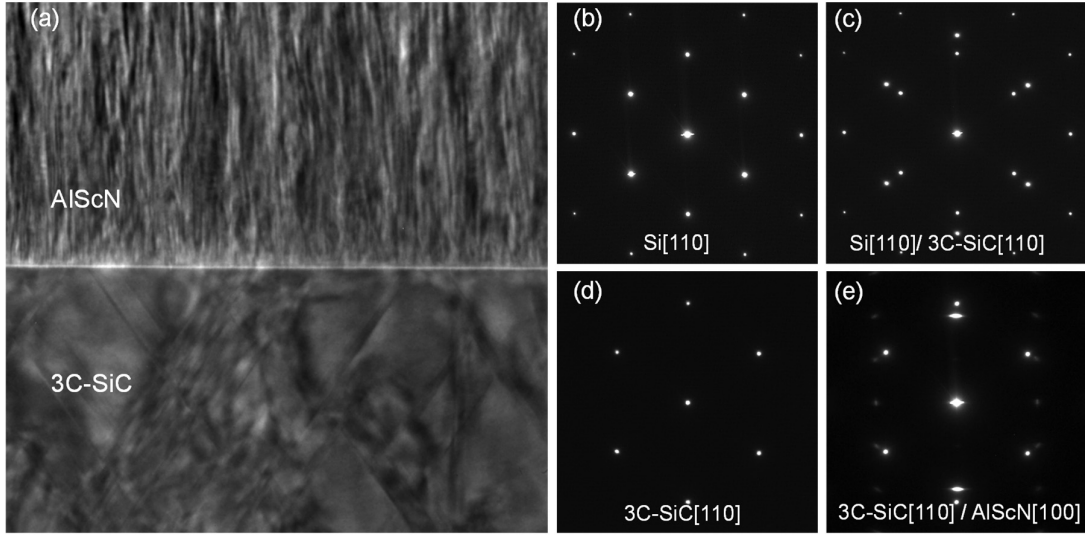


Figure S2. (a) TEM crosssectional image of the AlScN/3C-SiC interface. SAED patterns of (b) Si, (c) 3C-SiC, (d) 3C-SiC/Si, and (e) 3C-SiC/AlScN in the [110] orientation.

3. Temperature Coefficient of Resonance Frequency (TCf) of Circular Diaphragm

The multimode resonance frequency of circular diaphragm resonators can be expressed as [1]

$$f_n = \left(\frac{k_n r}{2\pi} \right) \sqrt{\frac{D}{\rho t r^4} \left[(k_n r)^2 + \frac{\gamma r^2}{D} \right]}, \quad (\text{S1})$$

where n denotes the mode number, ρ is the material mass density, t is the device thickness, $(k_n r)^2$ is the numerically calculated modal parameter, r is the radius of circular diaphragm, γ refers to the built-in tension (in [N/m], or stress [N/m² or Pa] times thickness), and D is the flexural rigidity, $D = E_Y t^3 / [12(1 - \nu^2)]$ in which E_Y and ν are Young's modulus and Poisson's ratio, respectively. **Equation S1** yields a mixed elasticity model, in which both flexural rigidity (dominated by the thickness and elastic modulus) and built-in tension (stress) play key roles in determining the resonance frequency.

3.1 Tension Dominant Limit

When $\gamma r^2 / D$ is very large and dominates in Equation S1, Equation S1 goes in the membrane regime, in which the frequency is dominated by the built-in tension,

$$f_n = \left(\frac{k_n r}{2} \right) \sqrt{\frac{\gamma}{\pi m}} = \left(\frac{k_n r}{2} \right) \sqrt{\frac{\sigma t}{\pi m}}, \quad (\text{S2})$$

where $\gamma = \sigma t$, and mass $m = \rho \pi r^2 t$. Both stress σ and thickness t are temperature dependent. To simplify the calculation, we assume the numerically calculated modal parameter, $(k_{nr})^2$, is independent of temperature. We ignore the effect of temperature change on the Young's modulus. Thus, **Equation S2** can be expressed as

$$f_n = \left(\frac{k_n r}{2} \right) \sqrt{\frac{\sigma t}{\pi m}} = \left(\frac{k_n r}{2} \right) \sqrt{\frac{\sigma_0 t_0}{\pi m}} (1 + \alpha \Delta T)^{\frac{1}{2}} \left(1 - \frac{\alpha E_{Y0}}{\sigma_0} \Delta T \right)^{\frac{1}{2}}, \quad (\text{S3})$$

where ΔT indicates the change of temperature, σ_0 and t_0 are the stress and thickness of the diaphragm at the initial reference temperature, α is the thermal expansion coefficient, and E_{Y0} is the Young's modulus at reference temperature. We can obtain $\partial f_n / \partial T$ as

$$\frac{\partial f_n}{\partial T} = \left(\frac{k_n r}{2} \right) \sqrt{\frac{\sigma_0 t_0}{\pi m r}} \left[\frac{1}{2} \alpha (1 + \alpha \Delta T)^{-\frac{1}{2}} \left(1 - \frac{\alpha E_{Y0}}{\sigma_0} \Delta T \right)^{\frac{1}{2}} - \frac{\alpha E_{Y0}}{2 \sigma_0} \left(1 - \frac{\alpha E_{Y0}}{\sigma_0} \Delta T \right)^{-\frac{1}{2}} (1 + \alpha \Delta T)^{\frac{1}{2}} \right]. \quad (\text{S4})$$

TCf of tension dominant limit case can be derived as

$$(TCf)_n = \frac{1}{f_n} \frac{\partial f_n}{\partial T} = \frac{1}{2} \alpha (1 + \alpha \Delta T)^{-1} - \frac{\alpha E_{Y0}}{2 \sigma_0} \left(1 - \frac{\alpha E_{Y0}}{\sigma_0} \Delta T \right)^{-1}. \quad (\text{S5})$$

Because $\alpha \Delta T \ll 1$ and $\alpha E_{Y0} \Delta T \ll \sigma_0$, we can approximately obtain

$$(TCf)_n \approx \frac{\alpha}{2} - \frac{\alpha E_{Y0}}{2 \sigma_0}. \quad (\text{S6})$$

Thus, the TCf is determined by the thermal expansion coefficient, Young's modulus at reference temperature, and built-in stress for the tension dominant limit.

3.2 Flexural Rigidity Dominant Limit

As $\gamma r^2 / D$ goes very small and negligible in Equation S1, flexural rigidity dominates the frequency, *i.e.*, and the model approaches the plate regimes.

$$f_n = \frac{(k_n r)^2}{2r} \sqrt{\frac{D}{\pi m}}, \quad (\text{S6})$$

where $D=E_Y t^3/[12(1-\nu^2)]$. We assume the numerically calculated modal parameter, $(k_n r)^2$, is independent of temperature. When the temperature changes by ΔT , **Equation S6** can be expressed as

$$f_n = \frac{(k_n r)^2}{4\sqrt{3(1-\nu^2)}r} \sqrt{\frac{E_Y t^3}{\pi m}} = \frac{(k_n r)^2}{4\sqrt{3(1-\nu^2)}r} \sqrt{\frac{E_{Y0} t_0^3}{\pi m}} (1 + \alpha \Delta T)^{\frac{3}{2}} (1 + TCE_Y \cdot \Delta T)^{\frac{1}{2}}, \quad (\text{S8})$$

where TCE_Y is the temperature coefficient of Young's modulus. $\partial f_n / \partial T$ can be expressed as

$$\frac{\partial f_n}{\partial T} = \frac{(k_n r)^2}{4\sqrt{3(1-\nu^2)}r} \sqrt{\frac{E_{Y0} t_0^3}{\pi m}} \cdot \left[\frac{3}{2} \alpha (1 + \alpha \Delta T)^{\frac{1}{2}} (1 + TCE_Y \cdot \Delta T)^{\frac{1}{2}} + \frac{1}{2} TCE_Y (1 + TCE_Y \cdot \Delta T)^{-\frac{1}{2}} (1 + \alpha \Delta T)^{\frac{3}{2}} \right]. \quad (\text{S9})$$

TCf in the flexural rigidity dominant limit can be derived as

$$\begin{aligned} (TCf)_n &= \frac{1}{f_n} \frac{\partial f_n}{\partial T} = \frac{\left[\frac{3}{2} \alpha (1 + \alpha \Delta T)^{\frac{1}{2}} (1 + TCE_Y \cdot \Delta T)^{\frac{1}{2}} + \frac{1}{2} TCE_Y (1 + TCE_Y \cdot \Delta T)^{-\frac{1}{2}} (1 + \alpha \Delta T)^{\frac{3}{2}} \right]}{(1 + \alpha \Delta T)^{\frac{3}{2}} (1 + TCE_Y \cdot \Delta T)^{\frac{1}{2}}}. \\ &= \frac{3}{2} \alpha (1 + \alpha \Delta T)^{-1} + \frac{1}{2} TCE_Y (1 + TCE_Y \cdot \Delta T)^{-1} \end{aligned} \quad (\text{S10})$$

Because $\alpha \Delta T \ll 1$ and $TCE_Y \cdot \Delta T \ll 1$, we can approximately obtain

$$(TCf)_n \approx \frac{3}{2} \alpha + \frac{TCE_Y}{2}. \quad (\text{S11})$$

Thus, the TCf is determined by the thermal expansion coefficient and temperature coefficient of Young's modulus for the flexural rigidity dominant limit.

4. Temperature Calibration Based on Silicon Raman Thermometry

We regulate the temperature by using a customized heating and sensing system. First, the devices are tested from room temperature up to 600°C in 50°C intervals for the ramp up cycle. Subsequently, we gradually decrease the temperature in 50°C intervals back to room

temperature. At each temperature point, we wait ~20 minutes for the temperature to stabilize and then take the resonance measurements. **Figure S3** shows the relationship between set temperature and the actual temperature of the heater over time.

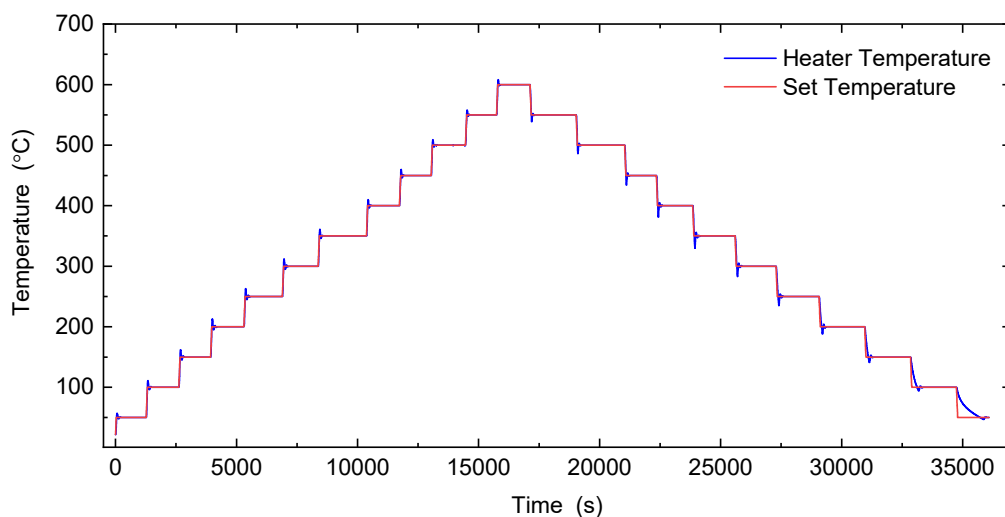


Figure S3. Temperature regulation measurement and calibration.

We utilize different clamps, including Ruthenium (Ru) probes, SUS340 clamping jig, and a ceramic piece, with enhancing thermal insulation for the sample, to mount the sample chip and calibrate the temperature based on the center position of Si Raman peak. The center peak position of Si Raman mode as a function of temperature for both heating and cooling cycles using different clamping methods are shown in **Figure S4** to **Figure S6**.

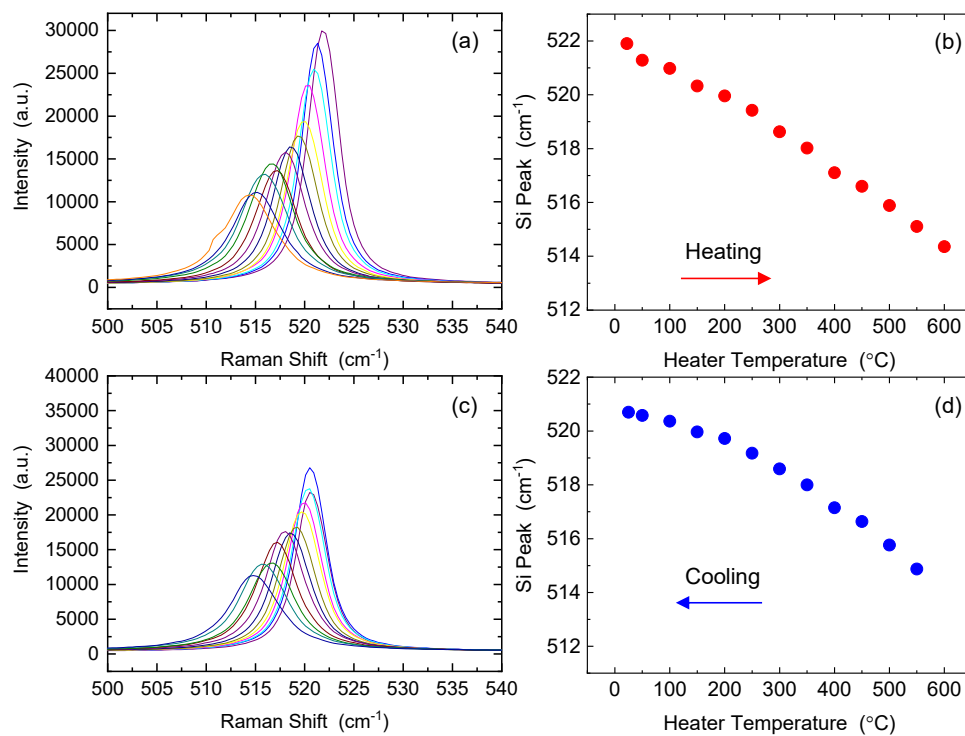


Figure S4. The center peak position of Si Raman mode as a function of temperature for both heating and cooling processes with the chip clamped by Ru probes.

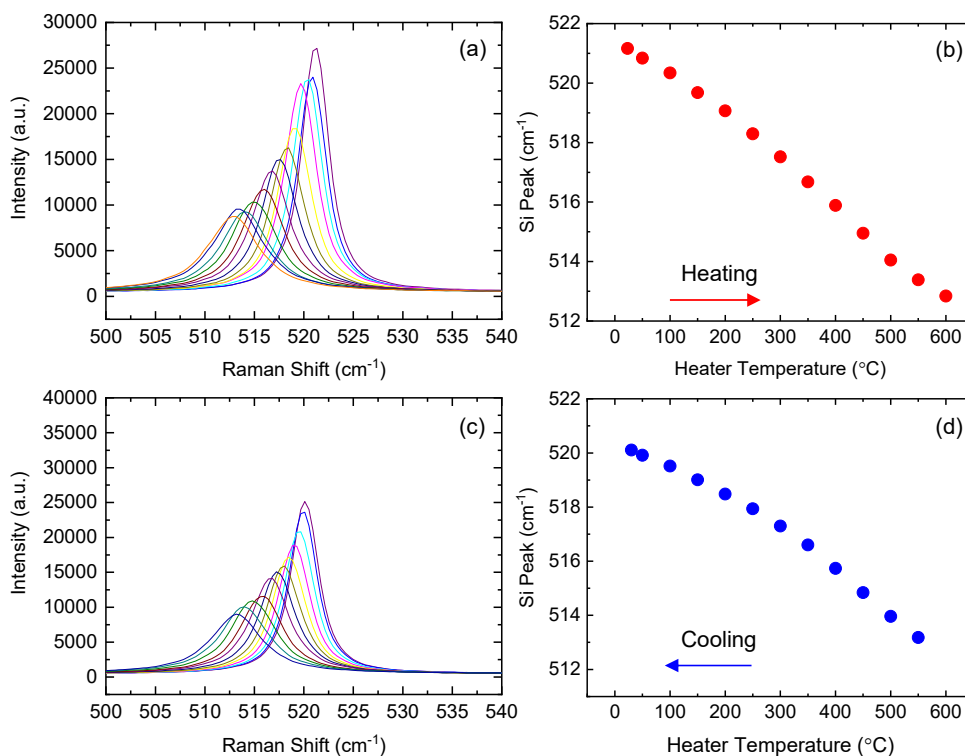


Figure S5. The center peak position of Si Raman mode as a function of temperature for both heating and cooling processes, with the chip mounted on heater and clamped by a SUS340 jig.

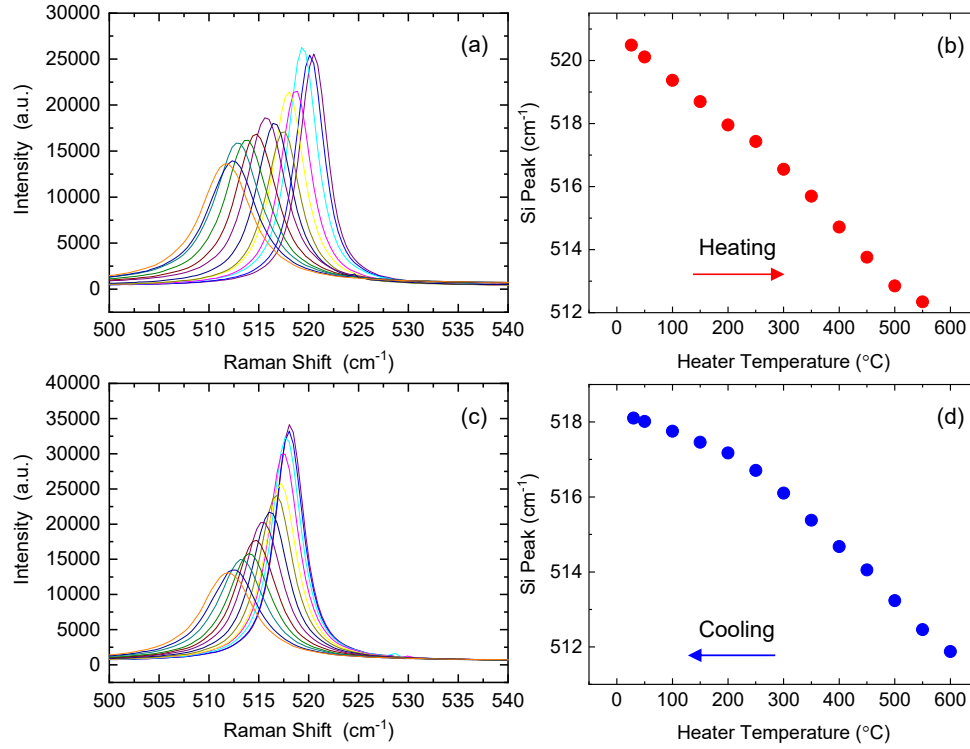


Figure S6. The center peak position of Si Raman mode as a function of temperature for both heating and cooling processes, with the chip clamped by a SUS340 jig and a ceramic piece onto the heater.

As shown in **Figure S7**, we refer to the temperature dependence of Raman scattering of the Si nanowires reported in [2] to calibrate the temperature read from Si Raman thermometry. When the chip is clamped by Ru probes, the temperature from Si Raman peak is $\sim 345^{\circ}\text{C}$ when the heater's set temperature is 600°C . Such a large temperature difference is probably due to the fairly large thermal conductivity of Ru ($\kappa \approx 151 \text{ W}/(\text{m}\cdot\text{K})$). We then further customize the design and expect the heating efficiency to be improved when the sample chip is clamped by SUS340 clamping jigs with $\kappa \approx 15\text{--}20 \text{ W}/(\text{m}\cdot\text{K})$. Further, we also insert a small piece of ceramic, with very low thermal conductivity of approximately $3.8 \text{ W}/(\text{m}\cdot\text{K})$, between the SUS340 clamping jig and the sample chip. Although we have expected a significant improvement in the thermal insulation and heating efficiency, only limited improvement is observed (see Figure S7). This may have resulted from the multi-point contact between the

ceramic piece and the chip; the considerably large effective contact area does not help minimize the heat transfer through the ceramic piece and the clamping jig, thus making the temperature of the chip and the devices lower than that of the heater (substrate).

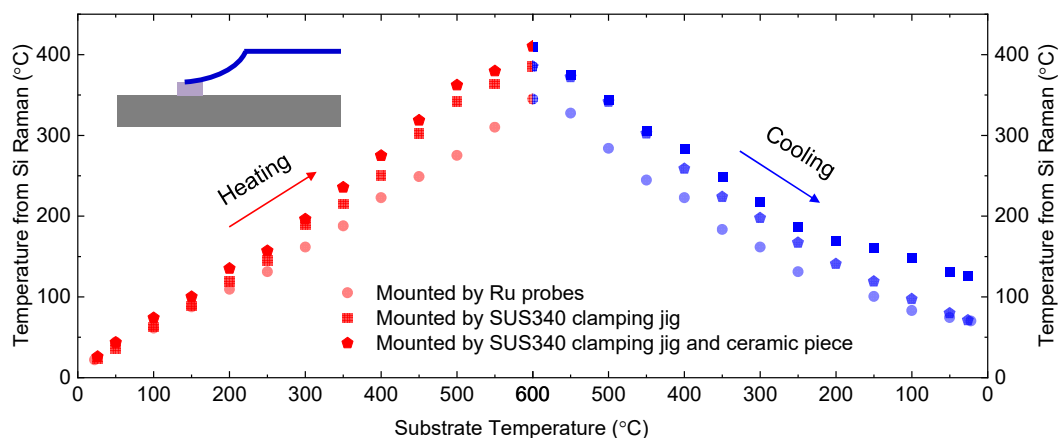


Figure S7. Temperature calibration based on Si Raman thermometry measured from the same chip mounted on the heater and clamped by Ru probes, SUS340 clamping jig and ceramic, respectively. The inset shows the diagram of the chip anchored by the SUS340 clamping jig and a ceramic piece.

5. Raman Spectroscopy Measurement with Varying Temperature

Figure S8 and **Figure S9** show the Raman spectroscopy results of the suspended AlScN/SiC measured with varying temperature, with the chip mounted on the heater and clamped by a SUS340 clamping jig alone, and by the SUS340 clamping jig with ceramic piece, respectively.

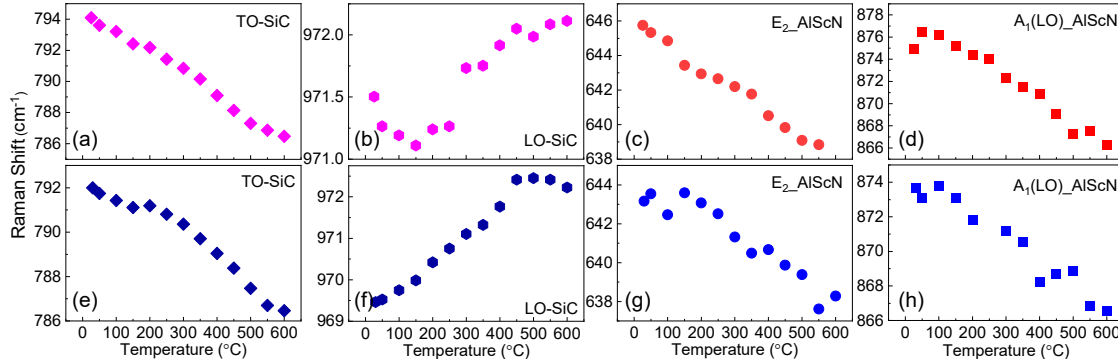


Figure S8. Raman spectroscopy results of suspended AlScN/SiC measured with varying temperature, with the chip clamped by a SUS340 clamping jig. Temperature dependence of the peak position of (a) $E_{2-AiScN}$ mode, (b) $A_{1(LO)-AlScN}$ mode, (c) TO_{SiC} , and (d) LO_{SiC} with temperature increasing from 25°C to 600°C. Temperature dependence of the peak position of (e) $E_{2-AiScN}$ mode, (f) $A_{1(LO)-AlScN}$ mode, (g) TO_{SiC} , and (h) LO_{SiC} with temperature decreasing from 600°C to 25°C.

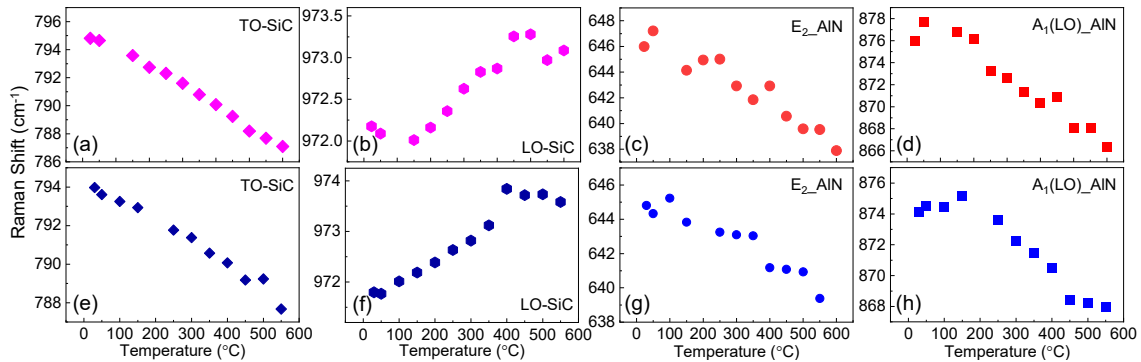


Figure S9. Raman spectroscopy results of suspended AlScN/SiC measured at varying temperatures with the chip mounted by SUS340 clamping jig and ceramic piece. Temperature dependence of the peak position of (a) $E_{2-AiScN}$ mode, (b) $A_{1(LO)-AlScN}$ mode, (c) TO_{SiC} , and (d) LO_{SiC} with temperature increasing from 25°C to 600°C. Temperature dependence of the peak position of (e) $E_{2-AiScN}$ mode, (f) $A_{1(LO)-AlScN}$ mode, (g) TO_{SiC} , and (h) LO_{SiC} with temperature decreasing from 600°C to 25°C.

References

- [1] H. Suzuki, N. Yamaguchi, and H. Izumi, *Acoust. Sci. Technol.*, **2009**, 30, 348-354.
- [2] S. Khachadorian, H. Scheel, A. Colli, A. Vierck, and C. Thomsen, *Phys. Status Solidi B*, **2010**, 247, 3084-3088.